ARTICLE

Sustainable by design large Stokes shift benzothiadiazole derivatives for efficient Luminescent Solar Concentrators

Received 00th January 20xx,
Accepted 00th January 20xx

DOI: 10.1039/x0xx00000x

Chiara Ceriani,†[a] Francesca Corsini,†[b] Giuseppe Mattioli,[c] Sara Mattiello,[a] Daniele Testa,[d] Riccardo Po,[d] Chiara Botta[e], Gianmarco Griffini,*[b] Luca Beverina*[a]

Luminescent solar concentrators (LSCs) are becoming an increasingly relevant topic in building integrated photovoltaic. Even if such devices are relatively simple planar waveguides doped with a luminescent material, the achievement of relevant efficiencies require a careful optimisation of both the matrix and the luminophore. Most of the recent literature focuses on the performance, yet the overall sustainability of the strategy is a topic at least as important. On this respect the luminophore plays a crucial role. Suitable materials must feature a near unit emission quantum yield, efficient light harvesting and a large separation between absorption and emission to reduce reabsorption losses. Due to the target application, such materials must also be readily available in large quantities and sustainable. Instead of going for performances first and scaling up/optimisation of the synthesis last, in this paper we offer a reversed perspective. We first designed and computationally characterised materials possessing structural features compatible with a green chemistry synthetic approach (micellar catalysis). Later on, we characterised the most promising materials in LSC devices and we compared performances with commercially available, non green chemistry compliant alternatives having similar spectral features. In the overall, we demonstrated comparable performances but greatly improved sustainability and scalability.

Introduction

Luminescent solar concentrators (LSCs)[1,2] are experiencing a major resurgence of interest. Originally investigated in the seventies when the increasing cost of silicon required alternative approaches, they remained below the radar for a long while for lack of performances. LSCs are now experiencing a rejuvenation due to important breakthroughs in the design of luminescent materials with suppressed reabsorption losses (large Stokes shift) enabling the fabrication of large area devices that are intrinsically suitable for building integrated photovoltaics. New device concepts for architectural integration of solar technologies such as LSC-based electrodeless photovoltaic (PV) windows are instrumental to the design of near-zero-energy buildings, a key feature to boost sustainability in densely populated areas.[3–5] A planar LSC consists of a high optical quality plastic or glass slab containing or coated by a luminescent material capable of absorbing sunlight and efficiently emit radiation, as much as possible down shifted to avoid reabsorption. Since the refractive index of the slab is higher than that of the air, most of the luminescence (depending on the refractive index mismatch between air and guiding material) is guided by total internal reflection to the LSC edges, where it is converted into electricity by efficient solar cells placed at the edges.[2,6] As the device is transparent, it can be flawlessly integrated in buildings with aesthetically pleasing effects.[7]

The choice of the guiding material is crucial in reducing the fraction of light escaping the waveguide and in reducing scattering and parasite absorption,[8] yet the core of a performing LSC is the luminescent material. The literature on such topic is vast and includes (a) well-established and industrially scaled up luminophores of the perylene bis imide family (Lumogen F Orange 240 and F Red 305) having high emission efficiencies but plagued by strong reabsorption losses;[9] (b) very high Stokes Shift but poor light harvesting UV-Vis absorption dyes and lanthanide complexes;[10–12] (c) inorganic and hybrid colloidal quantum dots;[13,14] and (d) NIR harvesting derivatives for transparent devices.[15] The research in the field is very active as the perfect luminophore capable of showing performances and low cost is still missing. Of course, the luminophore is just one of the three main elements of the LSC, also comprising the host material (PMMA) and the external PV modules. The industrial cost of PMMA is around 4 h per kg. The concentration of the dye is generally between 100 and 200

[a] Department of Materials Science, University of Milano-Bicocca, Via R. Cozzi, 55, Milano, Italy.
[b] Department of Chemistry Materials and Chemical Engineering "Giulio Natta", Politecnico di Milano, Piazza Leonardo da Vinci 32, 20133 Milano, Italy.
[c] CNR - Istituto di Struttura della Materia, Area della Ricerca di Roma, I-00015 Monterotondo Scalo, Italy.
[d] Eni Renewable Energy, Magnetic Fusion and Material Science Research Center,
[e] ENI S.p.A., via G. Fauser 4, 28100 Novara, ItalyCNR - Istituto di Scienze e Tecnologie Chimiche "Giulio Natta", via Corti 12, 20133 Milano, Italy.
† C. Ceriani and F. Corsini contributed equally to the reserach.
Electronic Supplementary Information (ESI) available: [details of any supplementary information available should be included here]. See DOI: 10.1039/x0xx00000x

ppm. Referring to the price of Lumogen dyes, the only industrially scaled dyes available for the application, this translates into 10–20 h per kg of PMMA.[16] The cost of the external PV modules is constantly decreasing but, at the time of this writing, averaged around 70 h per kg of slab. Overall, the cost of the luminophore is not the main factor in the pricing of the technology but is not negligible either.

The design guidelines for the preparation of a performing chromophore are known:[17] the presence of a charge transfer interaction between donor and acceptor groups upon excitation,[18] planarity and extension of the conjugated bridge connecting molecular units[19] and bulky groups preventing aggregation are a common trait of performing materials having large Stokes shifts.[20] Yet there is a wide variability in the structures proposed as well as in the tortuousness and overall sustainability of the synthetic paths required. The field of conjugated materials for (opto)electronic applications is now past the stage of proof of concept and rapidly evolving towards scaling up and precompetitive evaluation. While at that stage, it is not infrequent that materials having excellent properties at lab scale, quite simply do not make sense while scaling up on the ground of cost and/or sustainability. The field of OPV devices represents a very good case study on this respect. [21–24] LSCs are no different in that, due to the target application, luminophores have to be exceptionally rugged and easily available due to the quantities involved.[3] While designing new chromophores, performances generally come first and scaling up is considered in a subsequent step. In this paper we decided to turn the table around and, while keeping in mind the general rules for high efficiency materials, we designed chromophores using a *de novo* approach based on structural simplicity, availability and cost of raw materials, sustainability and efficiency of synthetic procedures and adherence to the recommendations of green chemistry as prerequisites to the design of intrinsically scalable materials. Recently, some of us described the first application of such new design criteria to the preparation of efficient and sustainable LSCs having an optical quantum efficiency higher than 50%.[25] Although remarkable, such devices had a particularly poor light harvesting capability due to the nature of the luminophore we designed, a [1]benzothieno[3,2-b][1]benzothiophene (BTBT) derivative with limited conjugation length.

In this paper we extend our *de novo* synthesis and design approach to a series of high Stokes shift derivatives featuring at the same time large spectral separation, suitable emission efficiency and exceptionally easy and green synthetic access. The new luminophores are fully characterized both in solution and as the active components of small and large area LSCs, demonstrating performances exceeding those of Lumogen chromophores in the particularly sought large area devices.

Design and computational insight

Aiming at the development of high Stokes Shift derivatives, we focused our attention on Donor-Acceptor-Donor molecules featuring easily accessible building blocks we could combine through a straightforward, sustainable chemistry. 2,1,3-benzothiadiazole is an acceptor with a considerable track record as a building block in luminescent materials, and can be efficiently coupled with a variety of heteroaromatics, including the π-excessive thiophene.[26–32]

We particularly focused on the 4,7-dithien-2-yl-2,1,3-benzothiadiazole (DTB) structural motif. DTB features a sizeable high Stokes shift and high molar absorptivity.[33,34] It is a simpler analogue of the more performing but synthetically challenging benzothiadiazole bridged derivatives some of us introduced in the past.[35] Indeed, such diaryloxybenzoheterodiazole derivates proved to be exceedingly efficient but challenging in terms of accessibility due to the use of 4,7-Dibromo-5,6-difluoro-2,1,3-benzothiadiazole (DBBF) as the main starting material.[35]

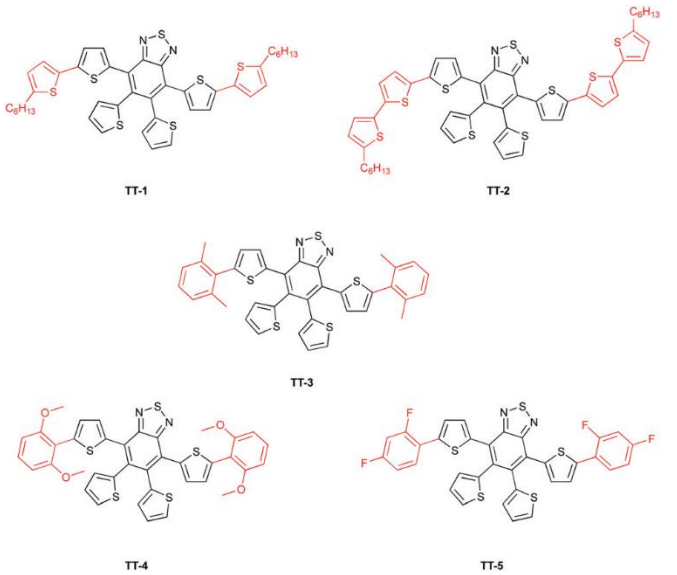

Scheme 1. Chemical structure of the new **TTB** luminophores

In this work, we propose a new class of benzothiadiazole bridged derivatives featuring 4,5,6,7-tetrathien-2-yl-2,1,3-benzothiadiazole core (**TTB**) as the most distinctive structural feature. The main advantage of such choice if the possibility to use the cheap and widely available 2,1,3-benzothiadiazole as the starting material and to proceed, at least up to a certain point in the synthesis, with a symmetric functionalization. We thus designed the three derivatives **TT1**, **TT2** and **TT3** as viable targets featuring properties suitable for LSC applications. Scheme 1. Prior to proceeding with the synthesis, we validated the design approach through a computational analysis.

The optimized geometries of the five investigated molecules are shown in Fig. 1, together with their frontier orbitals. The molecules are all characterized by a conjugated yet nonplanar structure, with the benzothiadiazole central unit forming solid angles with the 1,4 thiophene ''wings'' ranging from 351 in the case of TT2 to 471 in the case of TT3. All the molecules have HOMO orbitals widely distributed across the backbone, with features like those reported in the case of oligo- or polythiophenes, while LUMO orbitals are much more localized on the electron-acceptor benzothiadiazole central unit; the corresponding energy values are all listed in Table 1.

ARTICLE

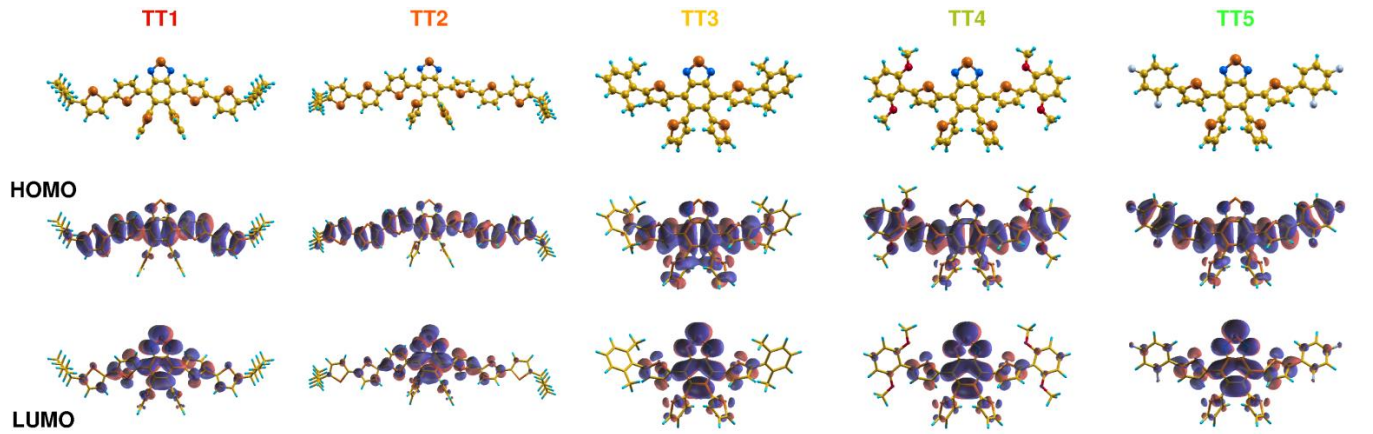

Figure 1. Calculated (B3LYP) Ground state geometries and HOMO and LUMO orbital densities for TT1-3 derivatives.

Table 1. Calculated HOMO, LUMO energies and Stokes Shifts according to both B3LYP and PBEh functionals.

	TT1	TT2	TT3
LUMO (eV)[a]	-2.64	-2.71	-2.65
HOMO (eV)[a]	-5.09	-4.95	-5.67
Eg (eV)[a]	2.45	2.24	3.02
S0→S1 (nm)[b]	460	481	391
λ-max (nm)[b]	465	486	396
Stokes' shift (cm^{-1})[b]	6456	6446	6308

[a] B3LYP; [b] PBEh3c

This kind of orbital partitioning in conjugated, twisted molecular structures is a prerequisite to observe strong absorption and large Stokes shift values. Regarding absorption, TDDFT vibronic spectra are shown in Fig. 2a. Strong S0-S1 transitions that can be observed for all the molecules between 350 and 600 nm, as also summarized in Table 1, arise from such spatial distribution of frontier orbitals: as exemplified in Fig. 2c in the case of TT1, a significant charge displacement from side thiophene units (blue regions undergoing charge depletion upon excitation) to the benzothiadiazole central core (red regions undergoing charge accumulation) is responsible for the sizable oscillator strength of such S0 - S1 electronic transitions.

TT2, featuring the largest conjugation, is characterized by the smallest optical gap in the series as well as by the strongest absorption intensity. TT3 is the most blue shifted of the series whilst TT1 absorption maximum falls in between those of TT2 and TT3. TT4 and TT5, whose MeO- and F- substituents extend frontier orbitals to the farthest phenyl groups, placed midway between TT3 and TT1.

Fig. 2b shows TDDFT normalized vibronic absorption and emission spectra, anticipating large Stokes shifts in all cases, as also reported in Table 1. As we will discuss in the optical characterization paragraph, such data are slightly overestimated due to the large contribution of exact-exchange (42%) to the PBEh functional we employed. This choice was dictated by the unsatisfactory results obtained with the B3LYP functional (20% of exact-exchange) in the description of charge-transfer excitations such as those which characterize the TT1–5 series.

Finally, hindered rotations of all 4 surrounding thiophene units are expected to prevent vibronic routes to non-radiative recombination of molecular excitation, thus anticipating a high fluorescence quantum yield. Such emission yield is also favoured by the strong absorption, which is not suppressed or even attenuated in the case of cofacial-like aggregation and is compatible with linear scaling of the maximum absorbance as a function of dye loading reported in Fig. 4. More specifically, large Stokes shift values are a consequence of the geometry changes occurring in the S0–S1 transition. As exemplified again in the case of TT1 (Fig. 2d), the a and b solid angles between benzothiadiazole and thiophene units and between two consecutive thiophene units, respectively, drop from values of 351 and 171 in the case of the ground state to values of 81 and 41 in the case of the S1 excited state. This results in an extended conjugation of the molecule, lowering the energy of the excited state and, in turn, inducing a red shift of the emission.

ARTICLE

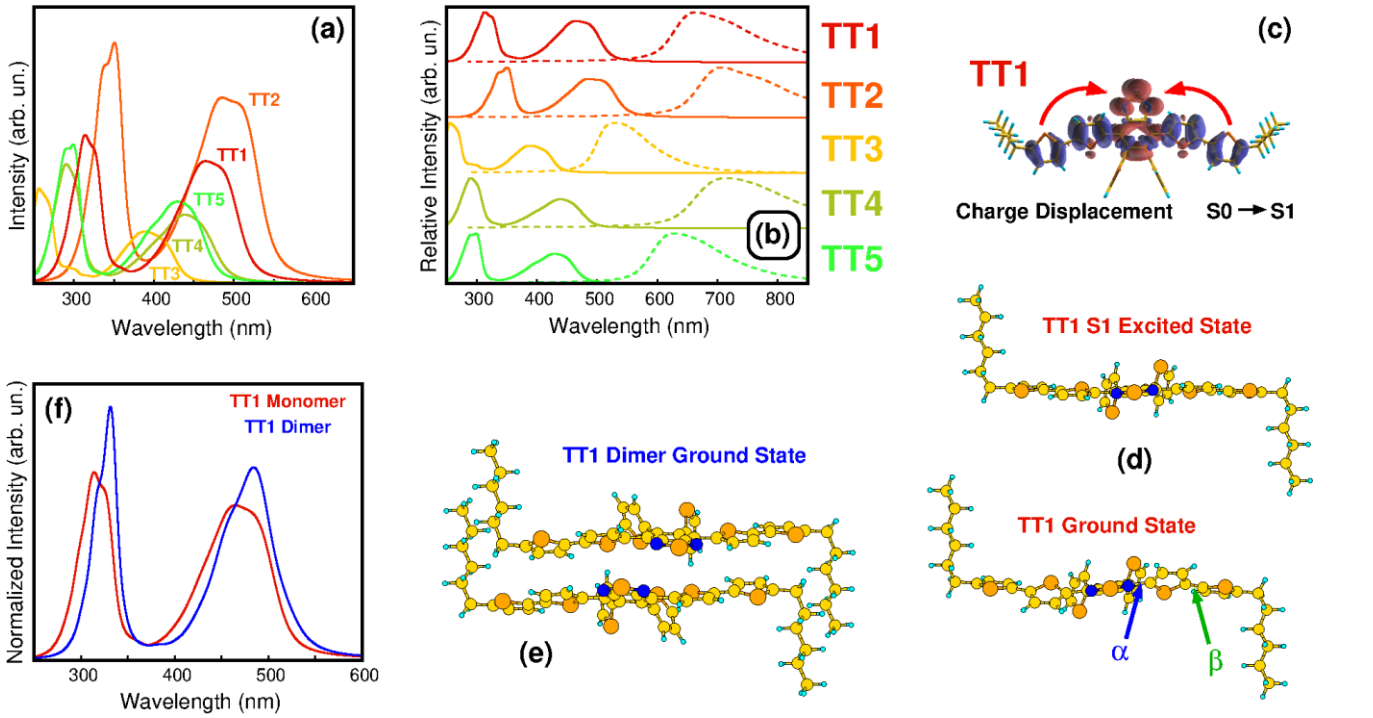

Figure 2. (a) TDDFT absorption spectra of TT1–5. (b) Relative absorption (solid lines) and emission (dashed lines) TDDFT spectra of TT1–5. (c) Density difference between S0 (ground state) and S1 (first singlet excited state) of TT1. Upon excitation, electronic charge is displaced from blue regions to red regions. (d) S0 and S1 optimized geometries of TT1; a and b are solid angles between the benzothiadiaziole unit and the first thiophene side ring, and between the first and second thiophene units, respectively. (e) Optimized geometry of a TT1 dimer. (f) Normalized TDDFT absorption of an isolated TT1 (red curve) and of a TT1 dimer (blue curve). All the calculations have been performed using the PBEh-3c functional..

Aggregation in the solid state may significantly alter the optoelectronic properties of molecular materials. We have simulated a simple TT1 dimer as a prototypical aggregate system. The optimized structure shown in Fig. 2e is the result of a large-scale exploration of configurations performed using tight-binding simulations and then refined using DFT-based simulations.Regarding the structural properties, we note that the strong interaction between large, conjugated aggregates induces a partial flattening of the a and b solid angles in the TT1 dimer. Such a structural feature is echoed in the normalized absorption spectrum plotted in Fig. 2f (blue curve), where both the main peaks are slightly red-shifted with respect to the isolated molecule, in suggestive agreement with the results obtained in the case of the high-concentration samples and discussed below.Having thus validated the design approach, we developed a sustainable synthesis protocol for the TTB family.

We based our approach on the guidelines of Green Chemistry, paying particular attention to the reduction of the E-Factor, a metric gaining relevant attention in industrial chemistry and corresponding to the ratio between the weight amount of the wastes produced (solvents and solids) and that of the product.[36] Accepted values in the field of pharmaceutical chemistry, the area where complexity of synthetic pathways is highest, are in the order of a few hundreds. In the context of organic semiconductors, such value is seldomly described but in general well in excess of several tens of thousands. On this respect, organic solvents are by far the most important source of waists. Over the last 10 years, micellar chemistry had a major impact on changing this scenario, convincingly demonstrating that the general hydrophobicity of organic products and intermediates does not represent a limit in the use of water as the main and often only solvent.[37–40] We have been amongst the first to apply the concept to the synthesis of conjugated molecules for printed electronics.[41–44]

Synthesis and evaluation of sustainability

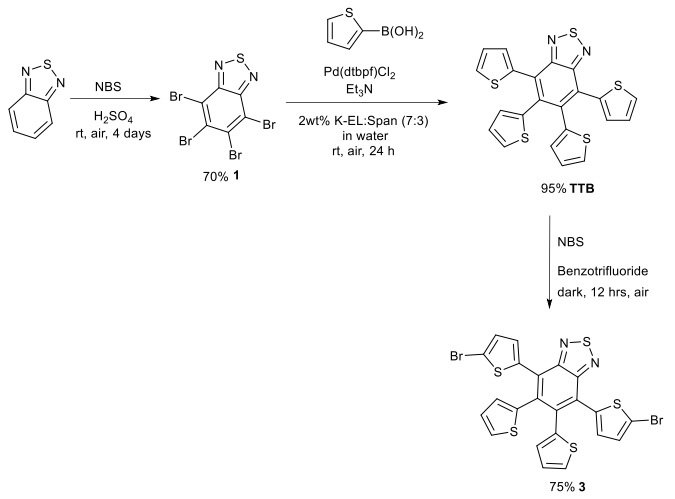

Scheme 2. General scheme for the synthesis of 4,5,6,7-Tetrakis(Thiophene-2-yl)-2,1,3-benzothiadiazole and 4,7-di(5-bromo-thiophene-2-yl)-5,6-di(thiophene-2-yl)-2,1,3-benzothiadiazole.

As it is shown in Scheme 2, our protocol starts with the tetrabromination of 2,1,3-benzothiadiazole, carried out in sulfuric acid in 70% yield. The resulting tetrabromobenzothiadiazole **1** was coupled with 4 equivalents of thiophene-2-boronic acid according to a S-M micellar reaction performed in a 2 wt% solution in water of a 7:3 wt/wt mixture of two industrial surfactants, Kolliphor EL (K-EL) and Span 80. The peculiar reaction medium was selected according to our previous experience with the coupling of 4,7-Dibromo-2,1,3-benzothiadiazole and thiophene-2-boronic acid.[44] The synthesis proceeds smoothly at room temperature and the purification involves an extractive crystallization in a Soxhlet apparatus requiring minimal amount of organic solvents. The thus prepared **TTB** core was already exploited as branching point for OPVs active molecules and can be recovered in essentially quantitative yield.[45]

Careful control of the reaction environment and conditions enabled the selective preparation of 4,7-di(5-bromo-thiophene-2-yl)-5,6-di(thiophene-2-yl)-2,1,3-benzothiadiazole **3**. Such kind of reactions generally require chlorinated solvents or aprotic dipolar ones like DMF. Industry is moving towards greener alternatives in order to minimize recurrence to toxic material.[46] We successfully profited of the good dissolving capabilities and remarkable chemical inertness of trifluorotoluene to carry out the reaction under mild conditions, allowing to recover the pure product by filtration in 75% yield. Intermediate **3** provided access to all the TTB derivatives, according to the same general reaction protocol shown in Scheme 3.

In this case, we exploited an emulsion S-M coupling (a strategy frequently defined as the co-solvent approach in the dedicated literature) instead of the micellar one. We previously observed that highly substituted and sterically crowded derivatives like bromide **3** do not react smoothly in aqueous micellar solutions due to the formation of sticky lumps.[47]

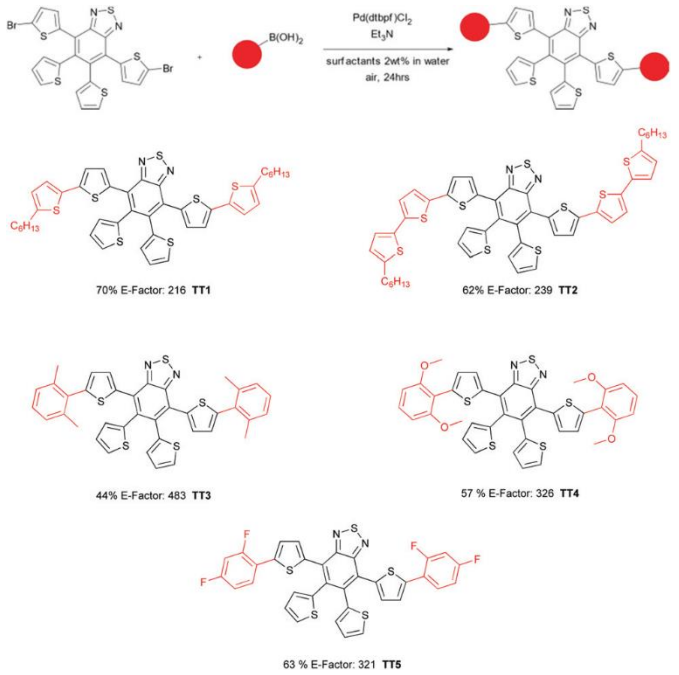

Scheme 3. General scheme for the synthesis of **TT1**-**TT5** chromophores. *The synthesis of this derivative was carried out at room temperature

To guarantee the correct dispersion of the reagents, a little amount of cosolvent (in less than stoichiometric amount with respect to the reagents), vigorous stirring and heating are needed in order to maintain the emulsion stable at all reaction stages. In order to demonstrate the generality of the approach we extended our protocol to derivatives involving boronic acids other than those directly leading to **TT1-3**. Only in the case of product **TT5** the reaction was carried out at room temperature to compensate the strong tendency to protodeborylation of 2,4-difluorophenylboronic acid.

In all the cases, processing required only minimal amounts of organic solvents, mostly employed in the final crystallization purification. Chromatographic purification was completely avoided in all reaction steps. We evaluated the E-Factor for the complete synthesis of all compounds, starting from 2,1,3-benzothiadiazole as the common raw material. The values range from 212 (derivative **TT1**) to 474 (derivative **TT3**), thus in all of the cases within the few hundreds typical of pharmaceutical chemistry. Such values makes it an even stronger case for the validity of our approach when compared with the value of 1192 recently estimated for the synthesis of the perylene derivative Lumogen R305, the standard luminophore for LSC applications.[25]

Photophysical properties

We carried out a preliminary optical characterization in solution for all **TTB** luminophores. Table 2 and Figure 3 summarize the main spectral characteristics of such compounds, to be compared with the computational values we previously discussed for **TT1-3** (Table 1). We also included the parent **TTB** core for comparison. We generally observed a good fit between

computational and experimental data. Coherently with the general features of Donor-Acceptor-Donor compounds, the optical gap of the various derivatives was largest for the parent unsubstituted **TTB** core and smallest for the more conjugated terthiophene functionalized **TT2**. The trend in the magnitude of the molar absorptivity closely follows the optical gap so that the larger values of the former are associated with the smaller ones of the latter.[48] With the notable exception of **TT2**, all derivatives possess high luminescence quantum yield, reaching near unit values for **TT3** and **TT5**. As derivatives **TT4** and **TT5** were not significantly different in terms of photophysical properties with respect to **TT1** and **TT3**, we did not include the formers in our LSC studies.

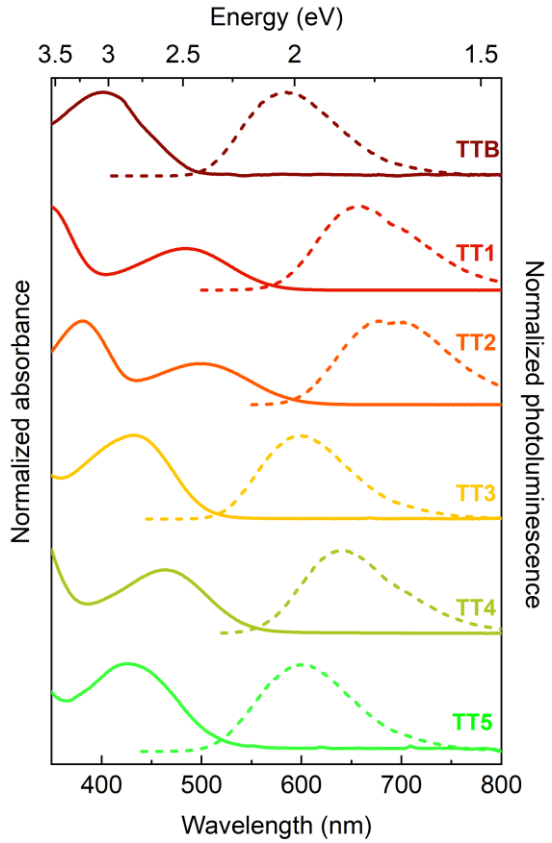

Figure 3. Normalized UV-Vis absorption (full lines) and emission (dashed lines) spectra in CH_2Cl_2 solution of **TT1-5** derivatives alongside with those of the **TTB** core.

Table 2. Optical Properties (Absorption and Emission Maxima, Stokes Shift, Molar Extinction Coefficient, and Photoluminescence Quantum Yield – PLQY) for Luminophores synthetized in CH_2Cl_2 solution

derivative	λ_{abs}(eV)/ λ_{abs}(nm)	λ_{em}(eV)/ λ_{em}(nm)	Stokes Shift (eV)	ε ($M^{-1}cm^{-1}$)	PLQY
TTB	3.09/401	2.13/582	0.96	8330	0.76
TT1	2.56/484	1.89/656	0.67	17700	0.71
TT2	2.48/500	1.83/677	0.74	39200	0.35
TT3	2.87/432	2.07/599	0.80	11240	0.99
TT4	2.67/464	1.94/639	0.73	10220	0.77
TT5	2.90/427	2.05/605	0.85	6170	0.99

Reabsorption-free LSC systems

We tested the performances of **TT1-3** in LSC devices using a thin-film architecture, where polymethyl methacrylate (PMMA) is the host matrix.[49]

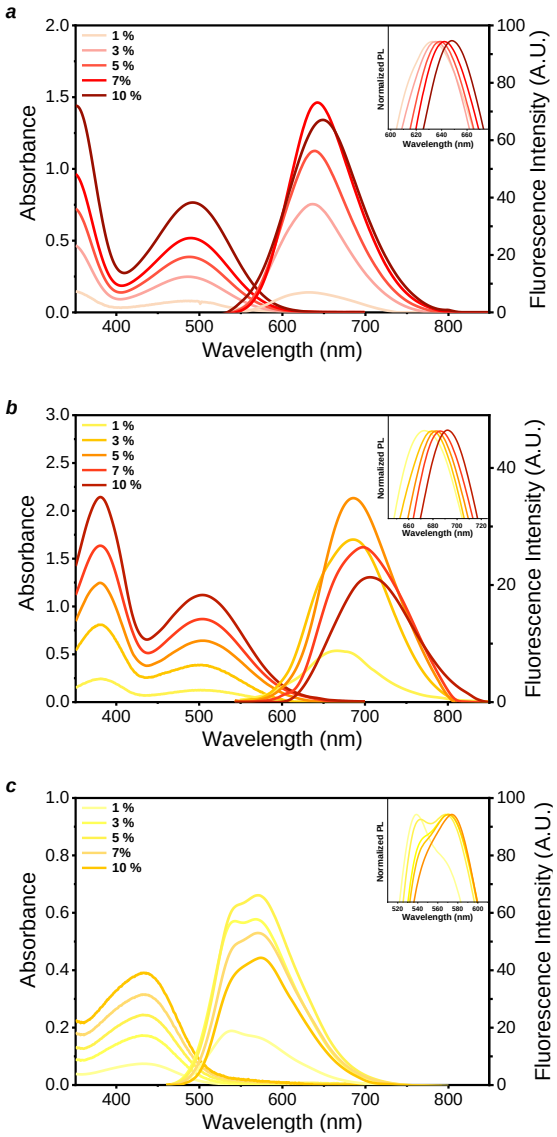

Figure 4. Absorption spectra and PL spectra recorded in the front-face-emission configuration at increasing luminophore concentrations of (a) **TT1**/PMMA LSCs (b) **TT2**/PMMA LSCs and (c) **TT3**/PMMA LSCs. In the inset: normalized PL spectra at increasing luminophore concentrations of (a) **TT1**/PMMA LSCs (λ_{exc} = 490 nm) (b) **TT2**/PMMA LSCs (λ_{exc} = 506 nm) and (c) **TT3**/PMMA LSCs (λ_{exc} = 434 nm).

Figure 4 shows the absorption and photoluminescence (PL) spectra in front-face configuration of the LSCs we prepared at increasing luminophore concentration (1 – 10 wt%). The absorbance grows linearly with luminophore concentration for all systems. The emission intensity grows steadily with luminophore loading up to a threshold concentration in the 5-7 wt% range. Above this limit, we observed a reduction in the PL intensity, accompanied by a bathochromic shift of the peak maximum (8, 14 and 26 nm for **TT3**, **TT1** and **TT2**). These trends suggest the presence of dissipative re-absorption phenomena

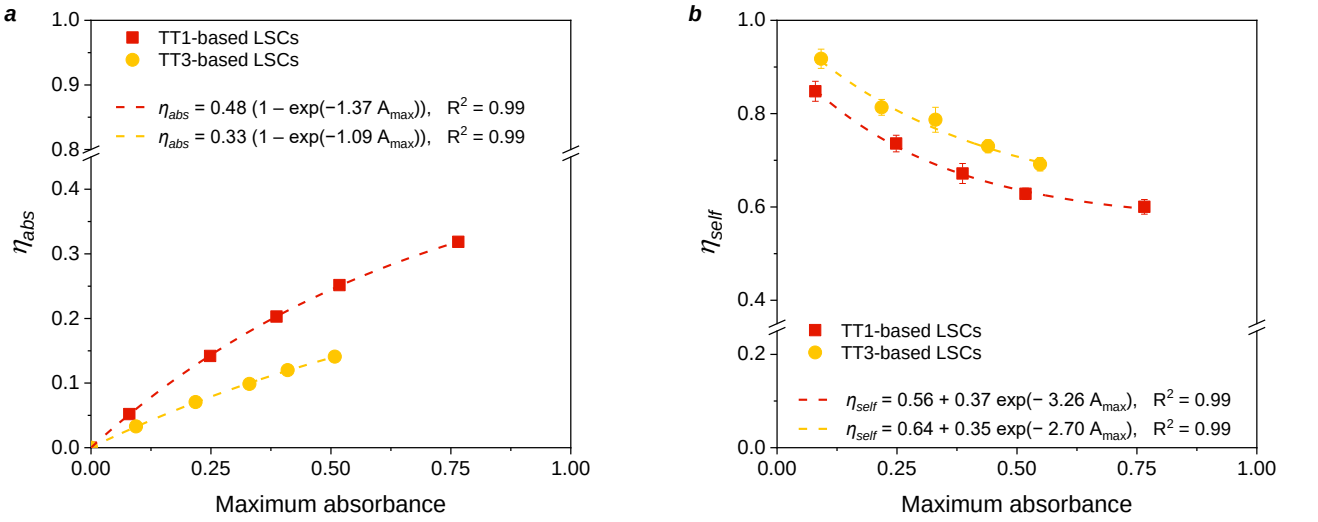

Figure 5. (a) η_{abs} of LSCs at maximum absorbance ($\lambda_{abs,max}$ = 434, 490 nm for **TT3** and **TT1**, respectively) in the wavelength range 300 – 800 nm. (b) Self-absorption efficiency of **TT3**- and **TT1**-based thin film LSCs (η_{self}) vs. maximum absorbance (*viz.*, luminophore concentration). The dashed lines represent the exponential fit to the experimental results. Fitting equations and related coefficients of determination are also displayed.

likely attributable to the slight overlap between absorption and emission spectra,[50] as will be discussed in the following paragraphs.

The relative PL intensity values we recorded for **TT2**/PMMA are very sizeably smaller than those of **TT1**/PMMA and **TT3**/PMMA at all concentrations. The differences in the relative emission quantum yields alone (Table 2), do not fully explain the phenomenon. The poor solubility of **TT2** could lead to the formation of crystalline dye aggregates in the PMMA film, quenching fluorescence and giving rise to non-negligible scattering losses (see Figure S2 in Section S10 of the ESI). We thus discarded **TT2**/PMMA LSCs from further analysis. Focusing on **TT1**- and **TT3**-based systems, we evaluated their absorption efficiency (η_{abs}) at each doping level as a quantitative measure of the match between the absorption response of the luminophore and the emission spectrum of the incident (solar) light ($\eta_{abs} \rightarrow 1$ should be sought for best match) (see Equation S2 in the ESI for details on calculations). In line with solution spectral properties, **TT1** outperformed **TT3** at all concentrations. In addition (Figure 5a), η_{abs} was found to gradually increase with absorbance, following an exponential trend in all systems. Also, at any given maximum absorbance, η_{abs} was found to be larger for **TT1** vs. **TT3** due to the greater overlap between the absorption spectra of the dye and the emission spectrum of the incident light source.

Low reabsorption losses are critical for high efficiency LSCs. We thus evaluated the self-absorption efficiency η_{self} at increasing dye loading as a function of maximum absorbance (see Equation E3 in the ESI). η_{self} provides a measure of the fraction of primary emitted photons reaching the edges of the LSC without being lost due to reabsorption events from neighbouring luminophore molecules ($\eta_{self} \rightarrow 1$ indicates no reabsorption effects). It is a parameter strictly related to the overlap between the absorption and emission spectra of the luminophore (the so-called radiative overlap, as discussed in Section S12 in the ESI).

Figure 5b shows that η_{self} follows an exponential decay with respect to optical density (A_{max}) (*viz.* luminophore concentration) for both derivatives, but **TT3**/PMMA consistently outperforms **TT1**/PMMA LSCs. Quite remarkably, η_{self} values found in these systems are significantly lower than those reported for benchmark LSCs doped with commercial organic dyes at comparable loading (e.g., highly concentrated devices based on PMMA embedding Lumogen F Red 305 (LR305 from here on) typically exhibit $\eta_{self} \approx 0.16 - 0.34$).[51,52] These evidences are key in highlighting the comparative advantages of using **TT1**,**3** dyes with respect to perylene dyes in LSCs.

LSC device performance and Monte Carlo ray-tracing modelling

We assessed the optical performance of lab-scale **TT1**- and **TT3**-based LSCs in terms of their external (η_{ext}) and internal (η_{int}) photon efficiency at increasing luminophore concentration (numerical values are listed in Table S2 in Section S13 of the ESI).[53]

TT1 exhibits higher η_{ext} vs. **TT3** at all doping levels, because of the more favourable match between the absorption spectra of this dye and the solar emission spectrum (*i.e.*, higher η_{abs}). In particular, we observed a maximum $\eta_{ext} \approx 5.0\%$ for **TT1**/PMMA LSCs, which is comparable with the highest values recently reported in the literature under similar irradiation conditions for luminophores having similar spectral response.[51,54] We obtained an opposite trend for η_{int}, comparatively prevailing for **TT3**/PMMA devices. This behaviour can be attributed to the larger η_{self} in **TT3** vs. **TT1**, which entails improved light guiding ability of the emitted photons given the intrinsically lower probability of reabsorption processes. The resulting maximum η_{int} ($\approx 40\%$) is among the best values reported in the literature for organic luminescent dyes.[25,55]

To better assess the extent of reabsorption losses and their effect on LSC response, we recorded the optical performance (integrated output power) of **TT1**- and **TT3**-based devices as a function of the distance between the excitation spot and the

collection edge (optical pathlength, *d*), as shown in Figure 6a. The output power remains in all cases constant for *d* higher than 5 cm, suggesting that for larger devices the emitted photons are able to propagate freely within the lightguide, thus reaching the collecting edge without significant optical losses (only a slight performance decrease at shorter distances was observed, mainly attributable to geometric effects). This behaviour can be associated with the negligible radiative overlap observed in these luminophores (Figure S3, Section S12 of the ESI), which strongly limits photon self-absorption phenomena. Interestingly, the minor role of reabsorption losses in **TT1** and **TT3** systems was further confirmed by the evolution of their normalized edge-collected optical power spectra, where no significant bathochromic shift of the emission peak was observed (Figure S5 in Section S13 of the ESI), as opposed to what is normally found in large-radiative-overlap, small-Stokes-shift luminophores such as Lumogen F Red 305.[52,56]

The suppression of reabsorption losses in our thin-film LSCs anticipates their potential for the fabrication of high-performance large-area devices. To validate this hypothesis, we performed Monte Carlo ray-tracing simulations to predictively model the optical response of **TT1**- and **TT3**-based LSC devices of increasing geometric gain *G* (defined as the ratio between top and edge surface area) in terms of η_{int}, η_{ext} and concentration factor $C = G \cdot \eta_{ext}$ (see Figure 6b,c). For benchmarking purposes, we also performed simulations on LR305-doped devices. **TT1**- and **TT3**-based LSCs displayed constant performance (both η_{int} and η_{ext}) for *G* values of up to ~50, thus confirming the negligible contribution of reabsorption losses to the overall optical response in these systems. Conversely, reference LR305-based devices exhibited a marked performance decline in the same range of *G* values, with η_{int} and η_{ext} decreasing by 25% and 20%, respectively. For larger devices, we observed a steady decrease of η_{int} and η_{ext} in **TT1** and **TT3** LSCs, mainly ascribable to light guide-related losses, resulting in a sublinear growth of *C* with *G*, until a saturation value was reached ($C = C_{sat}$, with C_{sat} being 37 and 24 for **TT1**- and **TT3**-based LSCs, respectively). However, when compared with benchmark LSCs based on LR305, both our new systems achieved C_{sat} at higher *G* values (*G* = 4200, 5500, and 2100 for **TT1**, **TT3** and LR305, respectively), due to weaker reabsorption losses. In addition, **TT1**-based devices displayed a higher C_{sat} value than LR305 systems (C_{sat} = 37 vs. 30), suggesting a higher maximum achievable output photon flux density. Interestingly, despite the comparatively lower PLQY (Table 1) and η_{abs}, **TT1**-based LSC devices outperformed LR305-based ones at higher *G* (> 500). Similarly, as a result of the highest η_{self} (Figure 5b), **TT3**-based LSCs exhibited the best η_{int} response for all *G* values considered (Figure 6c), ultimately indicating excellent cumulative performance in terms of luminophore emission properties and lightguide quality.[53] Experimental data obtained on LSC devices of up to *G* = 6.25 closely replicated the trends observed on modelled systems (Figure 6b,c), thus confirming the reliability of the simulation results.

Finally, to assess the application potential of these systems as integrated PV devices, we edge coupled to the glass substrate c-Si solar cells connected in series and we measured the light-to-electricity performance of the LSC-PV assemblies. The device efficiency (η_{dev}, Equation S8 in ESI for definition) was recorded at the optimum luminophore concentration (i.e., 5 wt% for **TT3**-based LSC and 7 wt% for **TT1**-based systems) in the presence of a dark absorbing background, without employing any reflective element at the free edges of the waveguide. In addition, a black mask was used on the LSC system to avoid direct illumination of the PV cells during testing.[53] In these experimental conditions, we measured values of η_{dev} = 0.51% and 0.30% for **TT1**- and **TT3**-based LSCs, which are only slightly lower than in LR305-doped thin-film LSCs, as the effect of reabsorption losses on device performance is known to be less detrimental at such small scale.[1,51,57] As expected, **TT1**/PMMA outperformed their **TT3**-based counterpart due to the better spectral match with the solar emission (*viz.*, higher η_{abs}). We calculated that with a 5 x 5 cm^2 **TT1**-LSC, our experimental set-up would yield a current of 12.6 mA and a maximum output power of 9.7 mW, which would be sufficient to feed low-power portable electronic devices.[58]

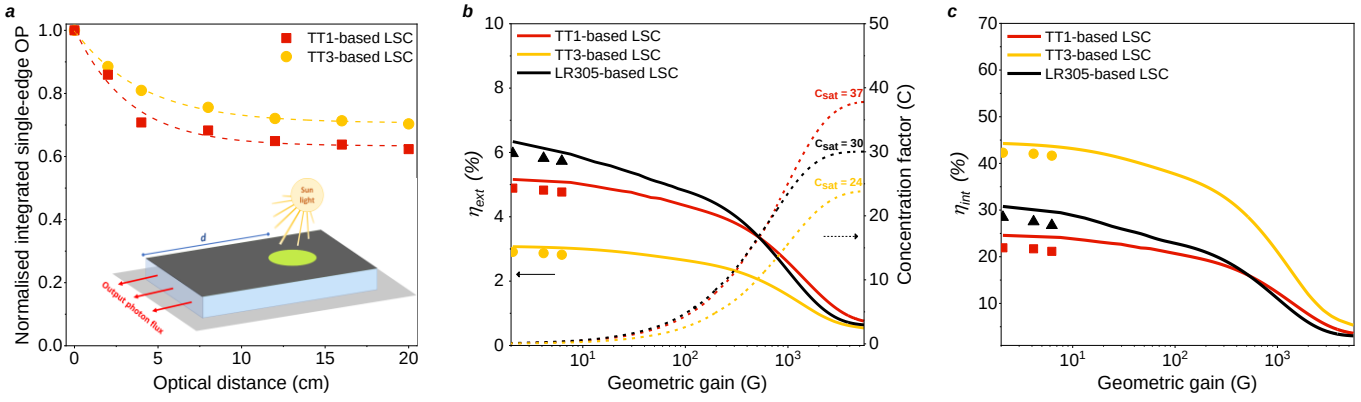

Figure 6 (a) Normalized integrated optical power output (OP) as a function of optical distance *d* under 1 sun top illumination of **TT3**- and **TT1**-based systems. The dashed lines indicate the fitting curves for **TT1** (fitting equation: OP=0.71+0.29·exp(-0.24·*d*), R^2=0.99) and **TT3** (fitting equation: OP=0.63+0.37·exp(-0.31·*d*), R^2=0.99). (b) Simulated η_{ext} (solid lines) and *C* (dashed lines) as a function of the geometric gain *G* for **TT3**-, **TT1**- and LR305-based LSC devices (the symbols indicate experimentally determined values). (c) Simulated η_{int} as a function of the geometric gain *G* for **TT3**-, **TT1**- and LR305-based LSC devices (the symbols indicate experimentally determined values).

Experimental Section

General Information

Reagents and solvents were bought from Apollo, Fluorochem, and Merk and used as received. PMMA (ALTUGLAS® BS 550) and index matching liquid 150 (IML150) were purchased from Arkema and Norland, respectively. Monocrystalline high efficiency silicon solar cells were provided by IXYS (IXOLAR SolarBIT KXOB22-12X1F, active area 2.2 × 0.6 cm^2, V_{OC} = 0.64 ± 0.01 V, J_{SC} = 42.60 ± 0.42 mA cm^{-2}, FF = 69.4 ± 0.3%, power conversion efficiency = 18.69 ± 0.23%). GC−MS spectra were collected on a Clarus 560 S PerkinElmer having an Elite-5MS 30.0 m × 250 µm column. Helium was used as carrier gas. NMR spectra were collected on a Bruker NMR Avance 400 NEO. Absorption spectra were collected on a Cary 60 UV−Vis Agilent spectrophotometer in a 10 mm path length quartz cuvette. Photoluminescence spectra were collected on a Cary Eclipse Fluorescence Agilent spectrophotometer in a 10 mm path length quartz cuvette. UV–visible absorption spectra of LSCs were recorded on a Thermo Scientific Evolution 600 UV–vis spectrophotometer using wavelength scan with a resolution of 1 nm at a scan speed of 120 nm/min and a slit width of 2 nm. The steady-state photoluminescence spectra were recorded both in front-face and edge emission configurations using a Jasco FP-6600 spectrofluorometer. The excitation wavelengths were 490, 506 and 434 nm for TT1, TT2 and TT3/PMMA LSC systems, respectively. To evaluate the optical performance of the considered thin-film LSCs, the systems were illuminated with an Abet Technologies Sun 2000 solar simulator, equipped with a Xenon lamp and an AM 1.5 filter. The output of the solar simulator was calibrated to 1 Sun (irradiance of 1000 ± 10 W m^{-2}). In this configuration, the solar simulator illuminates the top face of the LSC, which is placed on a black absorbing background. The spectrally-resolved optical power output at each edge of the LSC collected with a spectroradiometer (International Light Technologies ILT950) equipped with a cosine corrector positioned at the centre of the edge, while the other edges were covered with black tape. The optical power output spectra of the LSCs were recorded using SpectrILight III software. From these, the internal and external photon efficiencies were calculated. LSC device efficiency in the presence of edge-coupled c-Si solar cells was assessed using an Abet Technologies Sun 2000 solar simulator with AM1.5G filter and a Keithley 2612B source-measuring unit which allows to perform the voltage scans and measure the current output. I-V curves of the LSCs were recorded using LabView software and the data obtained were averaged out of at least three different devices.

Computational methods

Atomistic simulations of TTB derivatives have been carried out following a multi-level protocol. First, molecular rotamers have been sorted by using a semiempirical tight-binding approach, which has been also used in the case of TT1 dimer configurations; accurate optoelectronic properties were then calculated by using ab initio simulations. In the former case, the GFN2-xTB Hamiltonian[59] was used as ''engine'' for the search of minimum energy configurations through an automated conformer-rotamer ensemble sampling tool (CREST).[60,61] In the latter case, (timedependent) density functional theory simulations were performed in a GTO framework by using the ORCA suite of programs.[62,63] A more detailed description of computational methods has been enclosed in the ESI,† in order to ensure the full reproducibility of the calculations.

LSCs fabrication

Square-shaped LSCs of different sizes (5 × 5 × 0.6 cm3, 10 ×10 × 0.6 cm3 and 15 × 15 × 0.6 cm3) and rectangular-shaped LSCs with dimensions 20 × 5 × 0.6 cm3 were fabricated in thin film configuration (i.e., consisting of a slab of a high-opticalquality glass coated on one side with a host matrix/luminophore system). The substrates were made of a highoptical-quality glass (SCHOTT N-BK7).

A first analysis of the optical properties of TT1–3/PMMAbased LSCs as a function of the luminophore concentration was performed on devices with dimensions of 5 × 5 × 0.6 cm3. The devices were prepared starting from CHCl3 solutions of PMMA (10 wt%) with various concentrations of luminophore (expressed in wt% with respect to dry polymer). The TT1–3/PMMA films were obtained by spin coating (1000 rpm for 60 s) using a Laurell WS-400BZ-6NPP/LITE instrument. The average coatings thickness was measured by a KLA Tencor P-17 profilometer to be B3.5 mm.

On the basis of the findings of this preliminary investigation, large-area (10.0 × 10.0 × 0.6 cm3, 20.0 × 20.0 × 0.6 cm3 and 20 × 5 × 0.6 cm3) LSC devices with optimized luminophore concentration were fabricated using doctor-blade deposition technique. The PMMA powder was dissolved in a solvent mixture of 2:1 (v/v) chlorobenzene and chloroform to obtain a 6 wt% polymer solution. After 2 h magnetic stirring, the solution was deposited onto large-area glass plate via the doctor-blade technique.

For benchmarking purposes, we also fabricated and tested LR305-doped devices following the same procedures reported above. The LR305-based LSC devices were prepared varying LR305 concentration in the 1–10 wt% range with respect to dry polymer (PMMA).

To obtain LSC-PV systems, monocrystalline silicon solar cells connected in series were coupled to the LSC devices by means of IML150 low viscosity liquid monomer, so that two opposite edges of the glass substrates faced the photoactive area of two c-Si PV cells each.

Synthesis of 4,5,6,7-Tetrabromo-2,1,3-benzothiadiazole

In a 500 mL one necked round bottom flask equipped with calcium chloride valve, 2,1,3-Benzothiadiazole (3.30 g, 24.0 mmol) was dissolved in 100 mL of H_2SO_4. N-bromosuccinimide (21.4 g, 120 mmol) was slowly added portionwise. Reaction was stirred 4 days at room temperature. Reaction can be followed by GC-MS. Reaction was diluted in 200 ml of water, and precipitation of a solid was observed. The powder was filtered and washed with abundant solution of $NaHSO_3$, followed by

water until neutral pH. The as obtained product was dried in vacuum oven at 70 °C overnight. Straw yellow powder is recovered. 70% yield (7.58 g, 16.8 mmol). M.p. 225-227 °C (lit. 224-226)[64].
$^{13}C\{^{1}H\}$ NMR (100 MHz, $CDCl_3$): δ 151.93, 130.10, 117.60.

Synthesis of 4,5,6,7-tetrakis(thiophene-2-yl)-2,1,3-benzothiadiazole (TTB)

In a 500 mL two necked roundbottom equipped with a mechanical stirrer, 4,5,6,7-tetrabromo-2,1,3-benzothiadiazole (6.00 g, 13.2 mmol), $Pd(dtbpf)Cl_2$ (0.69 g, 1.05 mmol) and 2-thienylboronic acid (10.0 g, 79.0 mmol) were put under nitrogen atmosphere. 26 mL of 2 wt% aqueous degassed solution of Kolliphor EL:Span 80 (7:3) under stirring. After 5 minutes degassed $N(Et)_3$ (12.0 g, 118 mmol) was added, while keeping the temperature constant with a water bath. Reaction progress can be followed by GC-MS. After 24 hours the mixture was diluted with 50 mL of MeOH, and the obtained solid was filtered. The crude product was finally purified by extraction in Kumagawa apparatus using n-heptane. The pure product was recovered as a dark orange powder in 95% yield (5.84 g, 12.6 mmol). M.p. 278.6-282.0 °C.
^{1}H NMR (400 MHz, $CDCl_3$): δ 7.39-7.37 (m, 4H), 7.23 (dd ,2H, J = 5.1, 1.2 Hz), 7.04 (dd, 2H, J = 5.1, 3.7 Hz), 6.82 (dd, 2H, J = 5.1, 3.5 Hz), 6.73 (dd, 2H, J = 3.5, 1.2 Hz).
$^{13}C\{^{1}H\}$ NMR (100 MHz, $CDCl_3$): δ 154.00, 139.54, 137.22, 135.98, 130.57, 130.25, 127.86, 127.72, 127.29, 126.37.

Synthesis of 4,7-di(5-bromo-thiophene-2-yl)-5,6-di(thiophene-2-yl)-2,1,3-benzothiadiazole (product 2)

In a 100 mL roundbottom flask 4,5,6,7-Tetrakis(thiophene-2-yl)-2,1,3-benzothiadiazole (200 mg, 0.43 mmol) was dispersed in 20 mL of benzotrifluoride. *N*-Bromosuccinimide (160 mg, 0.89 mmol) was slowly added. Reaction was kept at room temperature in the dark for 24 hours. At the end of the reactions, 10 mL of EtOH were added and the obtained precipitate was filtered. The solid was washed with $NaHCO_3$ aqueous solution. Pure product was obtained as an orange powder in 75% yield (0,100 g, 0,16 mmol). M.p. 228.2-237.4 °C.
^{1}H NMR (400 MHz, $CDCl_3$): δ 7.28 (dd, J = 5.1, 1.2 Hz, 2H), 7.17 (d, J = 4.0 Hz, 2H), 6.97 (d, J = 4.0 Hz, 2H), 6.86 (dd, 1H, J = 5.2, 3.5 Hz 2H), 6.73 (dd, J = 3.6, 1.2 Hz 2H).
$^{13}C\{^{1}H\}$ NMR (100 MHz, $CDCl_3$): δ 153.52, 138.85, 138.75, 135.80, 131.19, 130.48, 129.33, 127.79, 126.90, 126.68, 115.66.

General Synthetic Procedure for SM coupling of Chromophores

Reactions were carried in a 10 mL round bottom test tube. 4,7-di(5-bromo-thiophene-2-yl)-5,6-di(thiophene-2-yl)2,1,3-benzothiadiazole (1 mmol), the boronic acid (3 mmol) and $Pd(dtbpf)Cl_2$ (0.04 mmol) were weighed in the test tube, and 2 mL of a 9:1 emulsion of aqueous 2 wt% solution Kolliphor EL and toluene was added. The mixture was stirred for 5 minutes at room temperature, then NEt_3 (6 mmol) was added. The reaction was warmed and kept at 60 °C for 24 h. Reaction was diluted with 10 mL of MeOH, and the solid was filtered. The crude was finally purified by crystallization.

TT1

The obtained solid was crystallized from heptane. A crystalline red powder was obtained. Isolated product: 70% yield (628 mg, 0.79 mmol). M.p. 126.3-134.2 °C.
^{1}H NMR (400 MHz, $CDCl_3$): δ 7.29 (d, 2H, J= 3.9 Hz), 7.27-7.26 (m, 2H), 7.01 (d, 2H, J= 3.9 Hz), 6.93 (d, 2H, J= 3.5 Hz), 6.85 (dd, 2H, J = 5.1, 3.5 Hz), 6.77 (dd, 2H, J = 3.5, 1.2 Hz), 6.65 (dt, 2H, J= 3.5, 0.9 Hz), 2.77 (t, 4H, J= 7.6 Hz), 1.70-1.63 (m, 4H), 1.40-1.26 (m, 12H), 0.89 (t, 6H, J= 7.0 Hz).
$^{13}C\{^{1}H\}$ NMR (100 MHz, $CDCl_3$): δ 153.79, 145.77, 140.57, 139.51, 135.56, 135.44, 134.50, 131.64, 130.36, 127.48, 127.16, 126.54, 124.75, 123.55, 122.37, 31.54, 30.17, 28.72, 22.55, 14.05.

TT2

The crude material was crystallized from toluene. A red powder was obtained. Isolated product: 62% yield (600 mg, 0.62 mmol). M.p. 186.5-196.8 °C.
^{1}H NMR (400 MHz, $CDCl_3$): δ 7.33 (d, 2H, J = 3.9 Hz), 7.29 (dd, 2H, J = 5.1 Hz, 1.2 Hz), 7.07 (d, 2H, J = 3.9 Hz), 7.01 (d, 2H, J = 3.8 Hz), 6.97-6.96 (m, 4H), 6.87 (dd, 2H, J = 5.1, 3.5 Hz), 6.78 (dd, 2H, J = 3.5, 1.2 Hz), 6.68 (d, 2H, J = 3.7 Hz), 2.79 (t, 4H, J = 7.6 Hz), 1.72-1.64 (m, 4H), 1.40-1.29 (m, 12H), 0.90 (t, 6H, J = 7.0 Hz).
$^{13}C\{^{1}H\}$ NMR (100 MHz, $CDCl_3$): δ 153.73, 145.72, 139.87, 139.39, 137.16, 136.15, 135.52, 135.18, 134.42, 131.83, 130.43, 127.61, 127.08, 126.62, 124.83, 124.45, 123.52, 123.42, 122.89, 31.55, 30.18, 28.74, 22.56, 14.07.

TT3

The crude material was crystallized from toluene. An orange powder is obtained. Isolated product: 44% yield (297 mg, 0.44 mmol). M.p. 218.0-225.0 °C.
^{1}H NMR (400 MHz, $CDCl_3$): δ 7.56 (d, 2H, J= 3.7 Hz), 7.23 (dd, 2H, J = 5.1, 1.2 Hz), 7.17-7.13 (m, 2H), 7.08-7.06 (m, 4H), 6.81 (dd, 2H, J = 5.1, 3.5 Hz), 6.78 (d, 2H, J= 3.6 Hz), 6.76 (dd, 2H, J = 3.5, 1.2 Hz), 2.13 (s, 12 H).
$^{13}C\{^{1}H\}$ NMR (100 MHz, $CDCl_3$): δ 153.91, 144.07, 139.80, 138.40, 137.69, 135.69, 133.70, 130.93, 130.52, 128.08, 127.58, 127.35, 127.15, 126.39, 125.67, 20.83.

TT4

The crude mixture was crystallized from heptane. An orange powder was obtained. Isolated product: 57% yield (470 mg, 0.64 mmol). M.p. 206.8-214.5 °C.
^{1}H NMR (400 MHz, $CDCl_3$): δ 7.52 (d, 2H, J = 3.9 Hz) 7.47 (d, 2H, J = 3.9 Hz), 7.26-7.24 (m, 2H), 7.19 (t, 2H, J = 8.3 Hz), 6.86-6.80 (m, 4H), 6.61 (d, 4H, J = 8.3 Hz), 3.80 (s, 12H).
$^{13}C\{^{1}H\}$ NMR (100 MHz, $CDCl_3$): δ 157.57, 154.10, 140.24, 137.00, 136.93, 135.16, 130.39, 129.94, 128.35, 128.31, 127.69, 127.04, 126.26, 112.61, 104.55, 55.85.

TT5

4,7-di(5-bromo-thiophene-2-yl)-5,6-di(thiophene-2-yl)-2,1,3-benzothiadiazole (622 mg, 1.00 mmol), 2,4-difluorophenylboronic acid (473 mg, 3.00 mmol), and $Pd(dtbpf)Cl_2$ (26.1 mg, 0.04 mmol) were weighed in the vessel, and then 2 mL of 2 wt % Kolliphor EL in water were added. The mixture was allowed to homogenize for 5 min before addition of NEt_3 (607 mg, 6.00 mmol). The reaction was stirred overnight at room temperature. The mixture was diluted with 10 mL of MeOH and filtered. The crude mixture was finally crystallized from heptane. A red powder was obtained. Isolated product: 63% yield (435 mg, 0.63 mmol). M.p. 318.8-325.0 °C.

^{1}H NMR (400 MHz, $CDCl_3$): δ 7.55-7.49 (m, 2H), 7.39 (dd, 2H, J = 3.9, 0.8 Hz), 7.34 (dd, 2H, J = 3.9, 1.4 Hz), 7.27 (dd, 2H, J = 5.1, 1.2 Hz), 6.90-6.85 (m, 6H), 6.79 (dd, 2H, J = 3.5, 1.2 Hz).

^{13}C{^{1}H} NMR (100 MHz, $CDCl_3$): δ 162.0 (dd, J = 250.0, 11.6 Hz), 159.2 (dd, J = 253.4, 11.6 Hz), 153.82, 139.35, 138.7 (d, J = 3.6 Hz), 137.4 (d, J = 3.6 Hz), 135.87, 131.50, 130.42, 129.45 (dd, J = 9.4, 5.1 Hz), 127.54, 127.31, 126.56, 125.56 (d, J = 6.5 Hz), 118.5 (dd, J = 13.1, 4.4 Hz), 111.7 (dd, J = 21.8, 3.7 Hz), 104.6 (t, J = 25.5 Hz).

^{19}F{^{1}H} NMR (376 MHz, $CDCl_3$): δ -108.9 (d, 7.9, 1H), -110.8 (d, 7.9 Hz, 1H).

Conclusions

We have applied a computationally aided *de novo* synthesis and design approach to develop a series of high Stokes shift derivatives featuring at the same time large spectral separation, high emission efficiency and exceptionally easy and green synthetic access. We have based our approach on the use of micellar catalysis as the key step in the tuning of the electronic structure of the new derivatives, employing a late-stage divergent functionalization strategy to connect molecular diversity with synthetic efficiency. All derivatives can be prepared efficiently, avoiding hazardous chemicals at all stages, and mostly relaying on water as the reaction medium. Amongst the 5 derivatives identified to be of potential interest as luminophores for LSCs, two preformed particularly well (**TT1** and **TT3**). We prepared thin film LSCs and carried out a detailed photophysical characterization, comparing the results with those obtained under similar experimental conditions with the standard in the field, the perylene dye LR305. The newly designed luminophores proved to be comparatively more performing, particularly for the large area devices that are key for the development of building integrated photovoltaics. The new luminophores are fully characterized both in solution and as the active components of small and large area LSCs, demonstrating performances exceeding those of Lumogen chromophores in the particularly sought large area devices. Such favourable spectral features, along with particularly contained E-Factors, makes **TT1** and **TT3** derivatives particularly good candidates for scaled up industrial applications.

References

1 J. Roncali, *Adv. Energy Mater.*, 2020, **10**, 2001907.
2 I. Papakonstantinou, M. Portnoi and M. G. Debije, *Adv. Energy Mater.*, 2021, **11**, 2002883.
3 N. Aste, M. Buzzetti, C. Del Pero, R. Fusco, F. Leonforte and D. Testa, *J. Clean. Prod.*, 2019, **219**, 35–45.
4 N. Aste, L. C. Tagliabue, C. Del Pero, D. Testa and R. Fusco, *Renew. Energy*, 2015, **76**, 330–337.
5 N. Aste, M. Buzzetti, C. Del Pero, R. Fusco, D. Testa and F. Leonforte, *Energy Procedia*, 2017, **105**, 967–972.
6 C. Yang and R. R. Lunt, *Adv. Opt. Mater.*, 2017, **5**, 1600851.
7 F. Meinardi, F. Bruni and S. Brovelli, *Nat. Rev. Mater.*, 2017, **2**, 1–9.
8 G. Griffini, *Front. Mater.*, 2019, **6**, 1–8.
9 F. Corsini, E. Tatsi, A. Colombo, C. Dragonetti, C. Botta, S. Turri and G. Griffini, *Nano Energy*, 2021, **80**, 105551.
10 C. Freund, W. Porzio, U. Giovanella, F. Vignali, M. Pasini, S. Destri, A. Mech, S. Di Pietro, L. Di Bari and P. Mineo, *Inorg. Chem.*, 2011, **50**, 5417–5429.
11 A. Sanguineti, A. Monguzzi, G. Vaccaro, F. Meinardi, E. Ronchi, M. Moret, U. Cosentino, G. Moro, R. Simonutti, M. Mauri, R. Tubino and L. Beverina, *Phys. Chem. Chem. Phys.*, 2012, **14**, 6452.
12 S. F. H. Correia, V. De Zea Bermudez, S. J. L. Ribeiro, P. S. André, R. A. S. Ferreira and L. D. Carlos, *J. Mater. Chem. A*, 2014, **2**, 5580–5596.
13 F. Meinardi, H. McDaniel, F. Carulli, A. Colombo, K. A. Velizhanin, N. S. Makarov, R. Simonutti, V. I. Klimov and S. Brovelli, *Nat. Nanotechnol.*, 2015, **10**, 878–885.
14 B. N. Pal, Y. Ghosh, S. Brovelli, R. Laocharoensuk, V. I. Klimov, J. A. Hollingsworth and H. Htoon, *Nano Lett.*, 2012, **12**, 331–336.
15 C. Yang, J. Zhang, W. T. Peng, W. Sheng, D. Liu, P. S. Kuttipillai, M. Young, M. R. Donahue, B. G. Levine, B. Borhan and R. R. Lunt, *Sci. Rep.*, 2018, **8**, 1–10.
16 Y. Li, J. Olsen, K. Nunez-Ortega and W.-J. Dong, *Sol. Energy*, 2016, **136**, 668–674.
17 M. G. Debije and P. P. C. Verbunt, *Adv. Energy Mater.*, 2012, **2**, 12–35.
18 R. Turrisi, A. Sanguineti, M. Sassi, B. Savoie, A. Takai, G. E. Patriarca, M. M. Salamone, R. Ruffo, G. Vaccaro, F. Meinardi, T. J. Marks, A. Facchetti and L. Beverina, *J. Mater. Chem. A*, 2015, **3**, 8045–8054.
19 A. Sanguineti, M. Sassi, R. Turrisi, R. Ruffo, G. Vaccaro, F. Meinardi and L. Beverina, *Chem. Commun.*, 2013, **49**, 1618.
20 J. Lucarelli, M. Lessi, C. Manzini, P. Minei, F. Bellina and A. Pucci, *Dyes Pigments*, 2016, **135**, 154–162.
21 C.-Y. Liao, Y.-T. Hsiao, K.-W. Tsai, N.-W. Teng, W.-L. Li, J.-L. Wu, J.-C. Kao, C.-C. Lee, C.-M. Yang, H.-S. Tan, K.-H. Chung and Y.-M. Chang, *Sol. RRL*, 2021, **5**, 2000749.
22 M. Moser, A. Wadsworth, N. Gasparini and I. McCulloch, *Adv. Energy Mater.*, 2021, **11**, 2100056.

23 A. Y. Al-Ahmad, F. Almayhi, M. F. Al-Mudhaffer, M. J. Griffith, W. Liu, S. Li, K. Sivunova, D. Elkington, N. A. Cooling, K. Feron, M. Shi, W. Belcher, H. Chen, P. Dastoor and T. R. Andersen, *Sustain. Energy Fuels*, 2020, **4**, 940–949.
24 R. Po, G. Bianchi, C. Carbonera and A. Pellegrino, *Macromolecules*, 2015, **48**, 453–461.
25 S. Mattiello, A. Sanzone, F. Bruni, M. Gandini, V. Pinchetti, A. Monguzzi, I. Facchinetti, R. Ruffo, F. Meinardi, G. Mattioli, M. Sassi, S. Brovelli and L. Beverina, *Joule*, 2020, **4**, 1988–2003.
26 Y. Wang and T. Michinobu, *J. Mater. Chem. C*, 2016, **4**, 6200–6214.
27 J. Du, M. C. Biewer and M. C. Stefan, *J. Mater. Chem. A*, 2016, **4**, 15771–15787.
28 B. A. D. Neto, A. A. M. Lapis, E. N. Da Silva Júnior and J. Dupont, *Eur. J. Org. Chem.*, 2013, 228–255.
29 US 8,846,942 B2, 2014.
30 S. Gao, B. Balan, K. Yoosaf, F. Monti, E. Bandini, A. Barbieri and N. Armaroli, *Chem. - Eur. J.*, 2020, **26**, 11013–11023.
31 US 9 ,923 ,113 B2, 2018.
32 C. Botta, P. Betti and M. Pasini, *J. Mater. Chem. A*, 2013, **1**, 510–514.
33 M. D'Alessandro, A. Amadei, I. Daidone, R. Po', A. Alessi and M. Aschi, *J. Phys. Chem. C*, 2013, **117**, 13785–13797.
34 B. Patrizi, A. Iagatti, L. Abbondanza, L. Bussotti, S. Zanardi, M. Salvalaggio, R. Fusco and P. Foggi, *J. Phys. Chem. C*, 2019, **123**, 5840–5852.
35 WO 2019138332 A1, 2019, 43pp.
36 P. Anastas and N. Eghbali, *Chem. Soc. Rev.*, 2010, **39**, 301–312.
37 S. Handa, Y. Wang, F. Gallou and B. H. Lipshutz, *Science*, 2015, **349**, 1087–1091.
38 S. Handa, M. P. Andersson, F. Gallou, J. Reilly and B. H. Lipshutz, *Angew. Chem. - Int. Ed.*, 2016, **55**, 4914–4918.
39 B. H. Lipshutz and A. R. Abela, *Org. Lett.*, 2008, **10**, 5329–5332.
40 B. H. Lipshutz, S. Ghorai, A. R. Abela, R. Moser, T. Nishikata, C. Duplais, R. D. Gaston and R. C. Gadwood, *J. Org. Chem.*, 2011, **76**, 4379–4391.
41 M. Sassi, S. Mattiello and L. Beverina, *Eur. J. Org. Chem.*, DOI:10.1002/ejoc.202000140.
42 A. Sanzone, A. Calascibetta, M. Monti, S. Mattiello, M. Sassi, F. Corsini, G. Griffini, M. Sommer and L. Beverina, *ACS Macro Lett.*, DOI:10.1021/acsmacrolett.0c00495.
43 S. Mattiello, M. Rooney, A. Sanzone, P. Brazzo, M. Sassi and L. Beverina, *Org. Lett.*, DOI:10.1021/acs.orglett.6b03817.
44 A. Sanzone, A. Calascibetta, E. Ghiglietti, C. Ceriani, G. Mattioli, S. Mattiello, M. Sassi and L. Beverina, *J. Org. Chem.*, 2018, **83**, acs.joc.8b02204.
45 Q. Li, C. Du, F. Li, Y. Zhou, M. Fahlman, Z. Bo and F. Zhang, *Chem. Mater.*, 2009, **21**, 5327–5334.
46 F. P. Byrne, S. Jin, G. Paggiola, T. H. M. Petchey, J. H. Clark, T. J. Farmer, A. J. Hunt, C. Robert McElroy and J. Sherwood, *Sustain. Chem. Process.*, 2016, **4**, 1–24.
47 M. Rooney, S. Mattiello, R. Stara, A. Sanzone, P. Brazzo, M. Sassi and L. Beverina, *Dyes Pigments*, 2018, **149**, 893–901.
48 D. G. Patel, F. Feng, Y. Y. Ohnishi, K. A. Abboud, S. Hirata, K. S. Schanze and J. R. Reynolds, *J. Am. Chem. Soc.*, 2012, **134**, 2599–2612.
49 E. Tatsi and G. Griffini, *Sol. Energy Mater. Sol. Cells*, 2019, **196**, 43–56.
50 G. Griffini, M. Levi and S. Turri, *Renew. Energy*, 2015, **78**, 288–294.
51 E. Tatsi, G. Fortunato, B. Rigatelli, G. Lyu, S. Turri, R. C. Evans and G. Griffini, *ACS Appl. Energy Mater.*, 2020, **3**, 1152–1160.
52 T. Dienel, C. Bauer, I. Dolamic and D. Brühwiler, *Sol. Energy*, 2010, **84**, 1366–1369.
53 M. G. Debije, R. C. Evans and G. Griffini, *Energy Environ. Sci.*, 2021, **14**, 293–301.
54 N. D. Bronstein, Y. Yao, L. Xu, E. O'Brien, A. S. Powers, V. E. Ferry, A. P. Alivisatos and R. G. Nuzzo, *ACS Photonics*, 2015, **2**, 1576–1583.
55 G. Lyu, J. Kendall, I. Meazzini, E. Preis, S. Bayseç, U. Scherf, S. Clément and R. C. Evans, *ACS Appl. Polym. Mater.*, 2019, **1**, 3039–3047.
56 Z. Krumer, W. G. J. H. M. van Sark, R. E. I. Schropp and C. de Mello Donegá, *Sol. Energy Mater. Sol. Cells*, 2017, **167**, 133–139.
57 O. M. ten Kate, K. M. Hooning and E. van der Kolk, *Appl. Opt.*, 2014, **53**, 5238.
58 Y. Liang, C.-Z. Zhao, H. Yuan, Y. Chen, W. Zhang, J.-Q. Huang, D. Yu, Y. Liu, M.-M. Titirici, Y.-L. Chueh, H. Yu and Q. Zhang, *InfoMat*, 2019, **1**, 6–32.
59 C. Bannwarth, S. Ehlert and S. Grimme, *J. Chem. Theory Comput.*, 2019, **15**, 1652–1671.
60 S. Grimme, *J. Chem. Theory Comput.*, 2019, **15**, 2847–2862.
61 P. Pracht, F. Bohle and S. Grimme, *Phys. Chem. Chem. Phys.*, 2020, **22**, 7169–7192.
62 F. Neese, *WIREs Comput. Mol. Sci.*, 2012, **2**, 73–78.
63 F. Neese, *WIREs Comput. Mol. Sci.*, 2018, **8**, e1327–e1327.
64 D. E. Hublitz, *J. Heterocycl. Chem.*, 1972, **9**, 539–540.

